Chemical Science

ROYAL SOCIETY OF CHEMISTRY

EDGE ARTICLE

View Article Online
View Journal | View Issue

Cite this: *Chem. Sci.*, 2025, **16**, 4066

All publication charges for this article have been paid for by the Royal Society of Chemistry

Colloidally uniform single-crystal precursors enable uniform $FAPbI_3$ films for efficient perovskite submodules†

Yugang Liang,[a] Yingping Fan,[a] Zhixiao Qin,[b] Lei Lu,[a] Haifei Wang,[a] Meng Ren,[a] Fang Liu,[a] Yanfeng Miao,[ac] Yuetian Chen *[ac] and Yixin Zhao *[acd]

With the unprecedented research development on lead halide perovskite photovoltaics, scaling up fabrication while comprehensively understanding the properties of cost-effective and highly uniform precursor films has become critical for their practical application. When enlarging the device area, good precursor purity serves as the first step in ensuring the uniformity of the perovskite film. Chemical purity and colloidal uniformity in the precursor solution both play important roles in dictating film uniformity and defect density. Here, for the first time, we explored the colloidal behavior of $FAPbI_3$ precursors using different preparatory materials of varied costs but with similar metal purity. As the colloidal size of regular PbI_2 + FAI powder precursors increased compared to that of PbI_2 colloids, the $FAPbI_3$ single-crystal precursor synthesized from low-purity chemicals exhibited a generally smaller and more uniform colloidal size, which yielded perovskite films with improved uniformity and reduced defect density at lower cost. The colloidally uniform single-crystal precursors led to photovoltaics with higher power conversion efficiency and better long-term operational stability. More importantly, the uniformity in the precursor and film was found to be beneficial for large-area fabrication, where the scaling-up production of 30 cm × 30 cm perovskite submodules based on single-crystal precursors achieved an impressive 20.7% efficiency.

Received 15th November 2024
Accepted 18th January 2025

DOI: 10.1039/d4sc07759h

rsc.li/chemical-science

Introduction

As a new generation of solar cells with bright industrialization prospects, perovskite solar cells have reached efficiency milestones comparable to crystalline silicon cells.[1–4] Up to now, the solution-based method, with its low manufacturing cost and high processability, has enabled the power conversion efficiency (PCE) of perovskite solar cells to reach 26.7%.[5–9] Specifically, the material formamidinium lead iodide ($FAPbI_3$) exhibits an optimal bandgap close to the Shockley–Queisser limit, showing great potential and excellent stability.[10,11] Unfortunately, for scaling-up manufacturing, the current heavy reliance on expensive high-purity lead halide and alkylammonium halide precursors could be a burden.[12–14] Meanwhile, using low-purity precursors, such as 98% lead iodide, is considered to have adverse effects on the crystallinity and charge carrier lifetime of the prepared perovskite films.[15–17] Moreover, efficiency loss from small-scale perovskite devices to large-area modules, along with poor reproducibility, is often reported even when using high-purity precursors.[18–22] Previous studies have also identified that good control of precursor chemistry enables the fabrication of pinhole-free and compact large-area perovskite films.[23–26] However, achieving spatial uniformity of perovskite films using precursor powder mixtures remains challenging as the area increases.[27] The obstacle to scalability lies in the inhomogeneous distribution of impurities, composition variations and defect density across different regions within the perovskite film.[26,28] Therefore, elucidating the relationship between solution chemistry and film uniformity is crucial for ensuring scalability in industrial applications.

Perovskite single crystals (SCs) of various compositions, such as $MAPbI_3$,[27,29] $FAPbI_3$,[30,31] $FASnI_3$,[32] and even two-dimensional perovskites,[33,34] with high purity and accurate stoichiometric ratios, have been used as precursor materials to ensure the reproducibility and cost-effectiveness of the fabricated photovoltaic devices.[6,35–37] The films prepared from perovskite SCs inherit the materials' notable characteristics, such as high

[a]*School of Environmental Science and Engineering, Frontiers Science Center for Transformative Molecules, Shanghai Jiao Tong University, Shanghai 200240, China. E-mail: yixin.zhao@sjtu.edu.cn; yuetian.chen@sjtu.edu.cn*

[b]*Shanghai Perovskite Technology Co., Ltd, Shanghai 201109, China*

[c]*Shanghai Non-carbon Energy Conversion and Utilization Institute, Shanghai 200240, China*

[d]*State Key Lab of Metal Matrix Composites, Shanghai Jiao Tong University, Shanghai 200240, China*

† Electronic supplementary information (ESI) available: Materials, experimental methods, and additional *J–V* curves, XRD, ICP-OES, SPO curves, PL, UV-vis, PL mapping, IPCE, TPV, EL spectra, dark current–voltage curves, certified *I–V* curves and statistical device parameters. See DOI: https://doi.org/10.1039/d4sc07759h

crystallinity, high purity, accurate stoichiometry, low trap density, and good stability.[28,32,38,39] However, a fundamental understanding of the solution chemistry of perovskite single-crystal precursors has not yet been well explored, which fails to provide constructive guidance for further improving film quality and device performance.

In this work, uniform $FAPbI_3$ perovskite films and devices of large areas are well achieved based on colloidally uniform single-crystal precursors. The economic viabilities of different $FAPbI_3$ precursors, including the PbI_2 + FAI powder and $FAPbI_3$ SCs, are investigated. The photovoltaic performance of the $FAPbI_3$ devices prepared using low-cost single crystals is compared to those prepared using halide salts with a purity exceeding 99.999%. The colloidal and chemical properties of these $FAPbI_3$ perovskite precursors are studied to elucidate the key factors contributing to the observed variations in the photovoltaic performance. The reproducibility and scalability of the $FAPbI_3$ perovskite films and devices based on these precursor materials are also explored. The challenge of inhomogeneity that arises during the scaling up of perovskite film fabrication is addressed by utilizing $FAPbI_3$ perovskite single-crystal precursors with the underlying colloidal behavior elucidated. More encouragingly, the feasibility of the colloidally uniform single-crystal precursor for scale-up promotion is demonstrated with an impressive 20.7% efficiency achieved on 30 cm × 30 cm (aperture area: 663 cm^2) perovskite submodules.

Results and discussion

Performance of $FAPbI_3$ single crystal-based films and devices

First, black-phase (α-) and yellow-phase (δ-) $FAPbI_3$ SCs were synthesized by inverse temperature crystallization (scheme in Fig. S1†) using just low-purity materials of 98% PbI_2 + synthesized FAI.[40,41] No impurities peaks were detected in the XRD patterns for both the δ-$FAPbI_3$ and α-$FAPbI_3$ SCs, confirming the high purity of the synthesized single crystals (Fig. S2†). To further assess the metal impurities in PbI_2 + FAI and single-crystal precursors, inductively coupled plasma optical emission spectrometry (ICP-OES) was utilized for the quantitative analysis of metal elements, such as Ca, K, and Na, which have been found to exert adverse effects on perovskite solar cell.[42] As shown in Fig. 1a, the feasibility of producing high-purity perovskite single crystals from low-purity preparatory materials is demonstrated by the significant inhibition of metallic residues. The amounts of these impurities in both the synthesized yellow- and black-phase perovskite single crystals are only subtly different from those found in the high-purity materials of 99.999% PbI_2 + 99.5% FAI, indicating the high purity of the single crystals. The nature of the perovskite SC synthesis can be regarded as a thermodynamically driven self-purification process.[43,44] Moreover, the mother liquor's high tolerance to impurities enables its recyclability for the production of single crystals. The purity of single crystals obtained from the circulating mother liquor was found to remain consistent with those obtained from the fresh solution (Fig. S3†). Cost analysis was conducted to assess the suitability of this SC-based method for commercial scale-up production, where the approximate cost difference when using single-crystal precursors was compared

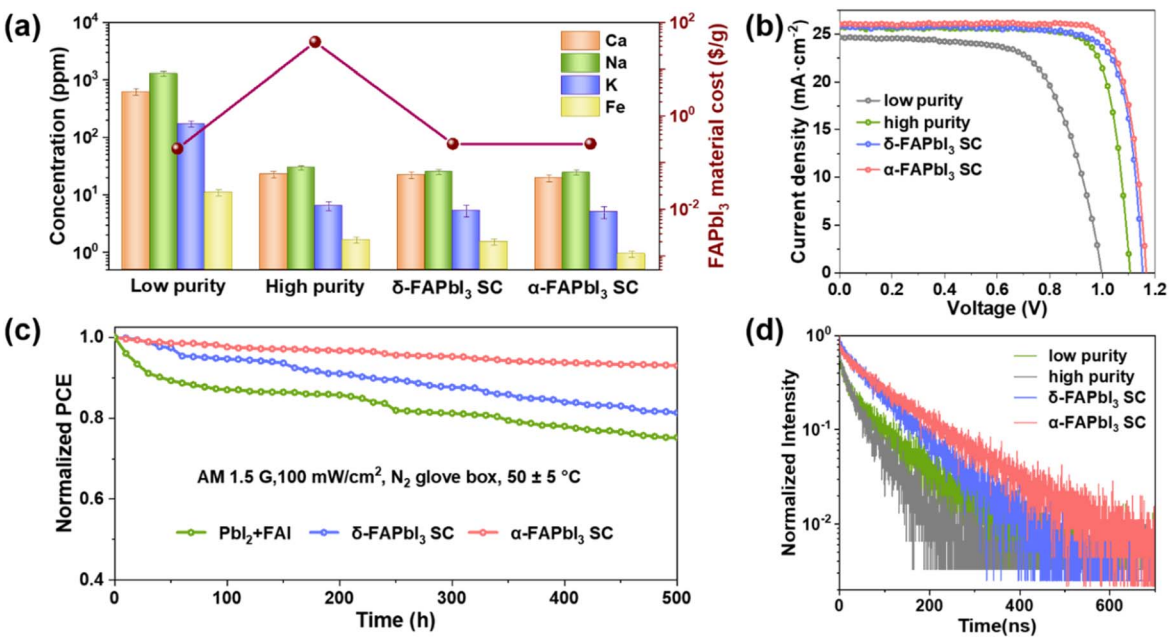

Fig. 1 Performance of films and devices based on different $FAPbI_3$ precursors. (a) Trace metal contents and material cost analysis for the low-purity, high-purity PbI_2 + FAI, synthesized δ-$FAPbI_3$ and α-$FAPbI_3$ SCs. (b) *J*–*V* curves of the best perovskite solar cells under reverse scans; (c) long-term operational stability of the devices based on PbI_2 + FAI, δ-$FAPbI_3$ and α-$FAPbI_3$ SCs; and (d) TRPL spectra of the perovskite films based on low- and high-purity PbI_2 + FAI, δ-$FAPbI_3$ and α-$FAPbI_3$ SCs.

to the existing precursors (Tables S1 and S2†). Considering the effect of temperature on the life of mother liquor, we estimated $FAPbI_3$ SCs at \$0.2478 per gram (δ-$FAPbI_3$ SCs for 15 cycles) and \$0.2492 per gram (α-$FAPbI_3$ SCs for 10 cycles), while low- and high-purity PbI_2 + FAI are \$0.196 and \$37.7 per gram, respectively (Fig. 1a). The implementation of the single-crystal precursor strategy has resulted in a remarkable reduction of about 150-fold in the manufacturing costs of PV devices.

To ascertain the comparability of the $FAPbI_3$ single-crystal precursor prepared from low-purity materials with conventional high-purity PbI_2 + FAI precursors, we prepared perovskite solar cells as the n–i–p configuration illustrated in Fig. S4.† The performance of perovskite solar cells based on traditional precursors PbI_2 + FAI is severely limited by the purity of lead iodide, which undoubtedly increases production costs (Fig. S5†). The presence of residual elements, such as Ca, K and Na, in the precursor can significantly compromise the performance of the device, which aligns with previous findings.[42] The encouraging discovery is that the $FAPbI_3$ SC-based perovskite solar cells with an area of 0.085 cm^2 exhibited greatly enhanced performance compared to those utilizing PbI_2 + FAI despite possessing similar purity of the precursors. Fig. 1b shows the current density (J)–voltage (V) curves of the PV devices based on α-$FAPbI_3$ and δ-$FAPbI_3$ SCs, where higher PCEs of 25.0% and 23.8% are exhibited when compared to 22.7% of the device based on high-purity PbI_2 + FAI. Moreover, the α-$FAPbI_3$ SC-based devices exhibit the lowest hysteresis index (HI), with a device V_{oc} of 1.17 V, short-circuit current density (J_{sc}) of 26.0 mA cm^{-2}, and fill factor (FF) of 82.4% (Fig. S6†). Better reproducibility of the devices fabricated from $FAPbI_3$ SCs is also revealed herein (Fig. S7†). The averaged open-circuit voltage (V_{oc}) value of these typical PV devices increases from 1.11 V for PbI_2 + FAI, to 1.14 V and 1.15 V for δ-$FAPbI_3$ and α-$FAPbI_3$ SCs, respectively (Fig. S8†). By integrating the external quantum efficiency (EQE) over the AM 1.5G standard spectrum, the projected J_{sc} of the PbI_2 + FAI, δ-$FAPbI_3$ and α-$FAPbI_3$ SC-based PSCs are 25.00, 25.38 and 25.46 mA cm^{-2}, respectively, which match well with the measured J_{sc} (Fig. S9†). Considering the manufacturing cost that relates to chemical purity, it is also worth noting that the PCE of the $FAPbI_3$ SC-based device does not significantly improve when using lead iodides of higher purity for the preparation of $FAPbI_3$ SCs (Fig. S10†). Moreover, Fig. S11† shows the stabilized power output (SPO) of the test device at the maximum power point. The same trend is that the maximum SPO value for the α-$FAPbI_3$ SC-based device is 24.66%, which is higher than that of 23.57% for the δ-$FAPbI_3$ SC-based device or 22.40% for the PbI_2 + FAI-based device. We monitored the operational stability of the devices using maximum power point (MPP) tracking under simulated 1-sun illumination, as depicted in Fig. 1c. The PCEs of devices based on α-$FAPbI_3$ and δ-$FAPbI_3$ SCs retained about 94% and 81% of their initial PCE after 500 h of MPP tracking, respectively, while that of PbI_2 + FAI rapidly declined to 75%.

The improvement in V_{oc} and stability of the devices could be ascribed to the reduction of defects in the perovskite film. Therefore, steady-state photoluminescence (PL) and time-resolved photoluminescence (TRPL) measurements were conducted to examine the trap density of the $FAPbI_3$ perovskite films prepared from different precursors. As shown in Fig. S12† and 1d, for the low- and high-purity PbI_2 + FAI precursors, the impurity concentration in the precursor significantly impacts both the PL intensity and carrier lifetime of the film. The reduction in calcium and sodium ions in the conventional PbI_2 + FAI precursor leads to fewer carrier trap states.[42] For the $FAPbI_3$ films based on both δ-$FAPbI_3$ and α-$FAPbI_3$ SC precursors, the PL intensities of the peak at around 810 nm are much stronger than those of high-purity PbI_2 + FAI. According to the TRPL data in Fig. 1d and Table S3,† the PL lifetime (τ) of α-$FAPbI_3$ SC-based film is much longer (122.82 ns) than that of δ-$FAPbI_3$ SC (88.89 ns) and high-purity PbI_2 + FAI (73.58 ns). The enhancement of PL intensity and lifetime indicates suppressed non-radiative recombination and reduced defect density in the $FAPbI_3$ SC precursor films. These results suggest that, apart from the metal ion purity, there must be some other differences in the properties between PbI_2 + FAI and $FAPbI_3$ single-crystal precursors to cause discrepancies in performance.

Origin of different $FAPbI_3$ precursor properties

To investigate the factors that contribute to the superiority of single-crystal-based device over traditional high-purity PbI_2 + FAI device, structural properties of the deposited perovskite films were analyzed by X-ray diffraction (XRD), scanning electron microscopy (SEM) and grazing-incidence wide-angle X-ray scattering (GIWAXS). Compared with the one based on PbI_2 + FAI precursor, the films prepared by δ-$FAPbI_3$ and α-$FAPbI_3$ SC precursors exhibit better crystallinity and higher phase purity (Fig. S13†). In addition, the residual lattice strain of the film can be evaluated by applying the Williamson–Hall (W–H) method[45,46] with data extracted from the XRD patterns. As the plots shown in Fig. S14,† the δ-$FAPbI_3$ and α-$FAPbI_3$ SC-based films exhibit lower lattice strain compared to the film based on PbI_2 + FAI. Moreover, the SEM images in Fig. 2a–c demonstrate that the $FAPbI_3$ SC precursor films exhibit larger and more uniform grain size (Fig. S15†), as well as smoother surface morphology compared to the PbI_2 + FAI precursor. Cross-sectional images also demonstrate that the single-crystal precursor can enable films with larger, intact and vertically grown grains. The GIWAXS results are shown in Fig. 2d. While PbI_2 residue (scattering vector of $q = 9$ nm^{-1}) is observed in the sample of PbI_2 + FAI film, the films based on single-crystal precursors exhibit a pure α-$FAPbI_3$ phase from either δ-$FAPbI_3$ or α-$FAPbI_3$ SCs. Fig. 2e shows that the single-crystal precursor films display a sharper peak near the azimuth angle of 90° after integrating the (100) diffraction intensity from the GIWAXS data, suggesting a more preferred crystallization along the vertical direction in these perovskite films. The results suggest that the different $FAPbI_3$ perovskite precursors, although with similarly high purity, could lead to the deposition of perovskite films exhibiting diverse structural profiles.

Comprehending the crystallization pathways of the different precursors is essential for identifying the causes of the distinct properties. As previously reported, the perovskite precursor solution is essentially a colloidal solution.[47] Therefore, to better study the $FAPbI_3$ single-crystal precursor and the traditional Pb_2

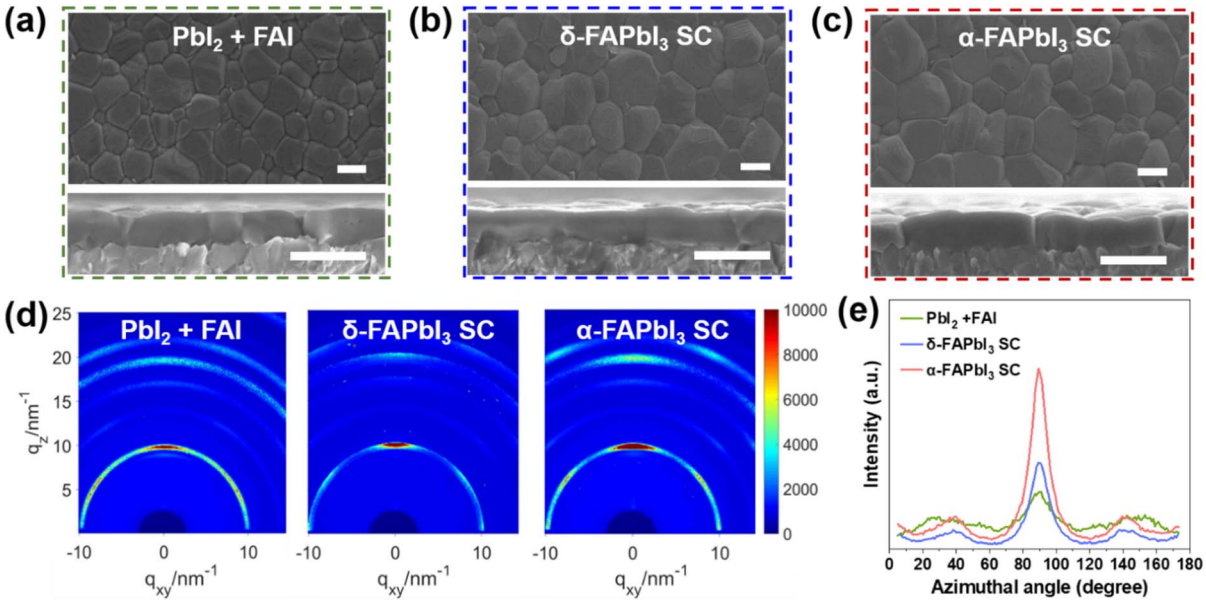

Fig. 2 Crystallinity of films based on different $FAPbI_3$ precursors. (a–c) Top-view (top) and cross-sectional (bottom) SEM images. Scale bars: 1 μm. (d) GIWAXS patterns and (e) derived azimuthal intensity profiles of the (100) peak of the $FAPbI_3$ perovskite films based on PbI_2 + FAI, δ-$FAPbI_3$ and α-$FAPbI_3$ SCs.

+ FAI precursor, the high-purity single crystals of δ-$FAPbI_3$ and α-$FAPbI_3$ were dissolved in solvents for use. Fig. 3a shows the UV-vis absorption spectra of the diluted precursor solutions that were prepared from PbI_2, PbI_2 + FAI mixture, δ-$FAPbI_3$ and α-$FAPbI_3$ SCs. The characterization was conducted immediately following the complete dissolution of different $FAPbI_3$ materials. The PbI_2 precursor exhibits a unique absorption peak at around 325 nm, which is considered the signature of low-valent

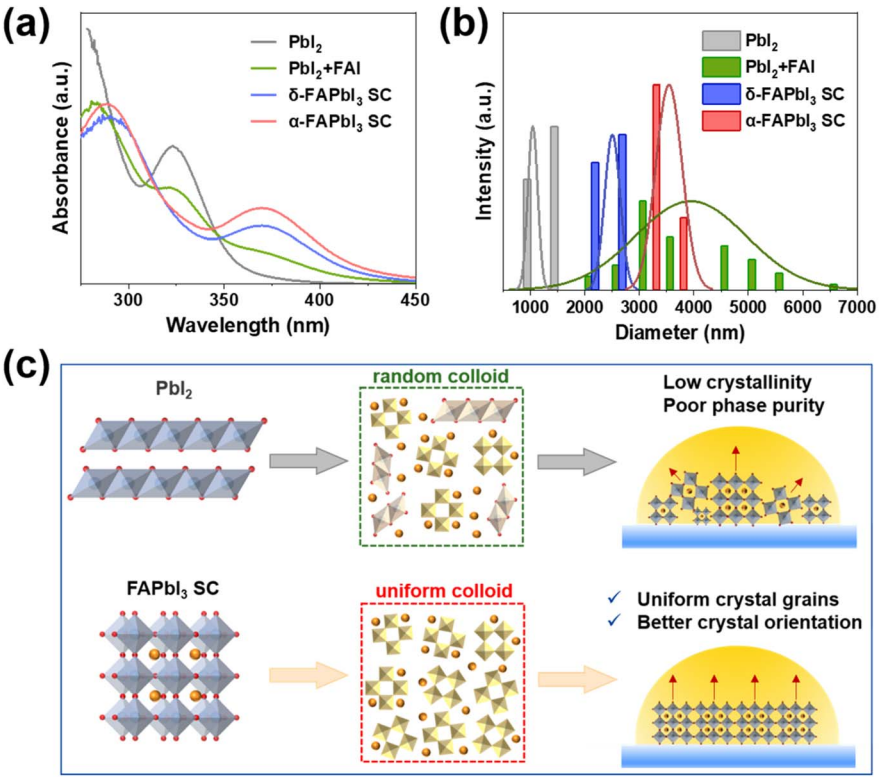

Fig. 3 Colloidal behaviors of different $FAPbI_3$ precursors. (a) UV-vis absorption spectra of diluted precursor solutions of PbI_2, PbI_2 + FAI, δ-$FAPbI_3$ and α-$FAPbI_3$ SCs. (b) Particle size distribution profiles of PbI_2, PbI_2 + FAI, δ-$FAPbI_3$ and α-$FAPbI_3$ SC precursors by DLS measurement. (c) Schematic of the crystallization mechanism of the different $FAPbI_3$ precursors.

iodoplumbate.[48,49] However, in the PbI_2 + FAI precursors, a gradual reduction in the intensity of this peak is observed with the increase in the FAI ratio (Fig. S16†), while the intensity on the characteristic peak of high-valent iodoplumbate at around 370 nm increases owing to the stronger coordination between Pb^{2+} and the incoming I^- ions.[49,50] Nevertheless, PbI_2 colloid with lower valence is still the dominant type of iodoplumbate in PbI_2 + FAI precursor. Interestingly, the absorption spectra of both δ-$FAPbI_3$ and α-$FAPbI_3$ SC precursor solutions exhibit only one signature peak of high-valent iodoplumbate at 370 nm, indicating that the chemical composition of the colloids in the precursor is highly uniform. Moreover, some studies have suggested that a high percentage of high-valent iodoplumbate in the precursor could act as the structural framework of the perovskite during crystallization, which would lead to better morphology and higher crystallinity of the deposited film.[27,29,32,33,51] Therefore, we then explored whether the $FAPbI_3$ precursors based on the PbI_2 + FAI mixture and $FAPbI_3$ SCs exhibit different colloidal behavior.

Dynamic light scattering (DLS) was used to measure the particle size distribution of the precursor. As shown in the profiles in Fig. 3b, the colloid size in the PbI_2 precursor has a limited range of 682–1398 nm, while that of the PbI_2 + FAI precursor varies significantly from 630 nm to 7000 nm, indicating an increase in the size of colloids in the PbI_2 + FAI precursor compared to PbI_2. The increase in colloid size and distribution range can be ascribed to the coordination between I^- and PbI_2 colloids to form iodoplumbate clusters. Different from the PbI_2 + FAI precursor, the δ-$FAPbI_3$ and α-$FAPbI_3$ SC precursors generally exhibit smaller colloids and a much narrower size distribution. The smaller colloid size is attributed to the dominance of the high-valent iodoplumbate with the highly uniform chemical composition,[52] suggesting that the dissolution of SCs into precursor solution exhibits a different colloidal behavior from the PbI_2 + FAI precursor.

These results confirm that uniform colloids containing high-valent iodoplumbate in $FAPbI_3$ SC precursor solutions serve as the structural framework for perovskite growth and facilitate the film formation of higher crystallinity. Meanwhile, the uniform distribution of colloids could yield crystal nuclei with similar growth kinetics during perovskite film formation.[53] Based on these results, it is concluded that in the $FAPbI_3$ SC precursors, the highly crystalline colloids composed of high-valent iodoplumbate could better promote the growth of highly ordered and uniform crystal grains, as revealed by the GIWAXS results and SEM images. Therefore, we propose a crystallization mechanism based on the behaviors of different $FAPbI_3$ precursors, as shown in Fig. 3c. For the PbI_2 + FAI, the precursor behavior leads to increased colloidal size and the formation of a random Pb–I skeleton with varied stoichiometry, which makes the assembled colloid clusters and the perovskite films have less crystallization orientation and poor phase purity. In contrast, the δ-$FAPbI_3$ and α-$FAPbI_3$ SC precursor solutions retain their pristine high-valent and uniform Pb–I skeleton colloid originated from single crystals, which yields the films with well-preserved highly oriented crystallinity.

The device was subjected to a series of characterizations to further assess the impact of different colloidal behaviors on performance. The non-radiative recombination caused by defects in the device can be quantitatively evaluated using the external quantum efficiency of electroluminescence (EQE_{EL}).[54] Fig. S17† shows an increasing trend in the electroluminescence (EL) intensity of the device based on PbI_2 + FAI, δ-$FAPbI_3$ and α-$FAPbI_3$ SCs. As revealed in Fig. 4a, under the injection current

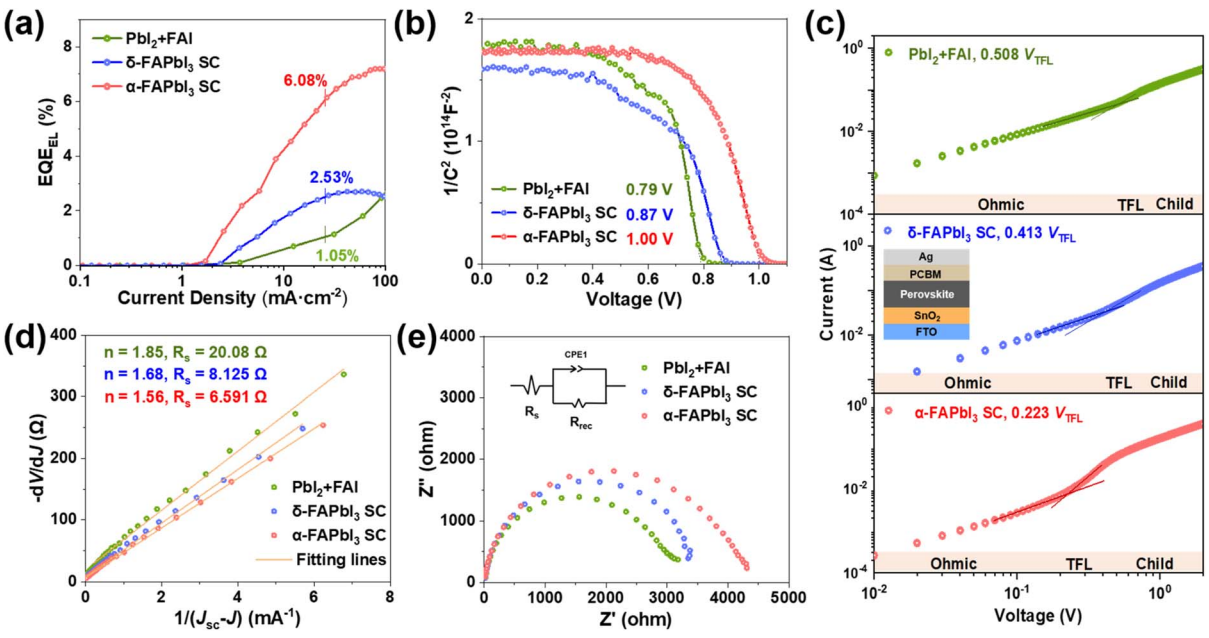

Fig. 4 Characterization of devices based on different $FAPbI_3$ precursors. (a) EQE_{EL}–current density curves, (b) Mott–Schottky plots, (c) dark I–V characteristics from SCLC measurements of the electron-only devices (structure shown as inset), (d) relationship between $-dV/dJ$ and $(J_{sc}-J)^{-1}$ in dark and (e) EIS data (fitting circuit model as inset) of the devices based on PbI_2 + FAI, δ-$FAPbI_3$ and α-$FAPbI_3$ SCs.

density corresponding to J_{sc}, the peak EQE_{EL} values of the device based on α-$FAPbI_3$ and δ-$FAPbI_3$ SCs were measured to be 6.08% and 2.53%, respectively, while that of the PbI_2 + FAI sample was 1.05%. We calculated the voltage loss due to non-radiative recombination ($\Delta V_{oc,\ non\text{-}rad}$), where the devices based on α-$FAPbI_3$ and δ-$FAPbI_3$ SCs exhibited lower $\Delta V_{oc,\ non\text{-}rad}$ of 0.069 V and 0.095 V than the PbI_2 + FAI (0.118 V), respectively, which is consistent with the V_{oc} difference in the *J*–*V* curves. Mott–Schottky plots (Fig. 4b) were used to further evaluate the charge-carrier dynamics in the prepared devices. The PbI_2 + FAI-based device reveals a low built-in potential (0.79 V), while the values for the δ-$FAPbI_3$ and α-$FAPbI_3$ SC-based devices increase to 0.87 V and 1.00 V, respectively. As shown in the space-charge limited current (SCLC) measurement in Fig. 4c, the trap-filled limit voltage (V_{TFL}) decreased from 0.508 V for PbI_2 + FAI to 0.413 V for δ-$FAPbI_3$ SC and 0.223 V for α-$FAPbI_3$ SC. The trap-state densities (n_{trap}) are calculated to be 3.54×10^{15}, 2.88×10^{15} and 1.55×10^{15} cm^{-3} for PbI_2 + FAI, δ-$FAPbI_3$ and α-$FAPbI_3$ SC-based devices, respectively. To better understand the origin of the enhanced V_{oc} in $FAPbI_3$ single crystal-based devices, a series of device comparisons were conducted with the results shown in Fig. 4d, S18 and S19.† As the relationship between effective voltage (V_{eff}) and photocurrent density (J_{ph}) shown in Fig. S18,† in the low V_{eff} region where J_{ph} is not saturated,[55,56] PbI_2 + FAI-based devices exhibit a lower photocurrent density than that of δ-$FAPbI_3$ and α-$FAPbI_3$ SC-based devices. The ideal factor (*n*) calculated from the relationship between $-dV/dJ$ and $(J_{sc}-J)^{-1}$ in Fig. 4d also indicates that the δ-$FAPbI_3$ and α-$FAPbI_3$ SC-based devices have higher charge-carrier transport capability. In addition, compared to conventional powder mixture precursors, the lowest saturation recombination current density (J_0) of the device based on α-$FAPbI_3$ SC precursor (Fig. S19†) further confirms its ability to suppress the non-radiative recombination that is associated with voltage loss. Transient photovoltage (TPV) decay (Fig. S20†) and electrochemical impedance spectroscopy (EIS) curves (Fig. 4e) also indicate that the devices based on single-crystal precursors have fewer defects than the PbI_2 + FAI device.

Single-crystal precursor for high-performance modules

To achieve scalable fabrication of perovskite devices with high performance, the uniformity of the films needs to be ensured. The PL mapping results of 2 cm × 2 cm $FAPbI_3$ perovskite films show that there is no significant difference in uniformity between perovskite films derived from single-crystal precursors and those derived from powder mixture precursors, except for the advantage of PL intensity (Fig. S21†). However, the differences between these perovskite films become more pronounced as the area increases. The $FAPbI_3$ single crystal-based samples also show more uniform UV-vis absorption profiles (Fig. 5a) than the PbI_2 + FAI mixture, regardless of different locations on the same 30 cm × 30 cm film. The variation of PL mapping intensity of PbI_2 + FAI and δ-$FAPbI_3$ SC precursor films in different locations is visualized in Fig. 5b and S22–S24.† The

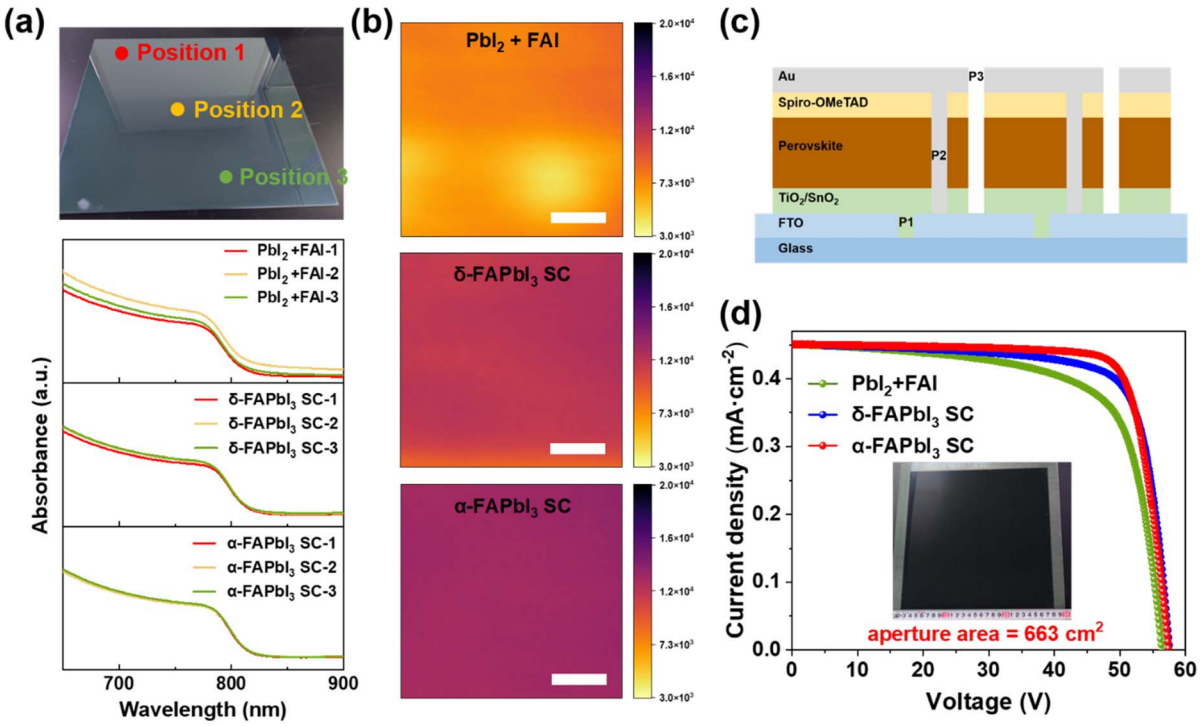

Fig. 5 Scalability of devices based on $FAPbI_3$ SC precursors. (a) UV-vis absorption spectra of different regions on 30 cm × 30 cm sized perovskite films based on PbI_2 + FAI, δ-$FAPbI_3$ and α-$FAPbI_3$ SCs. (b) PL mapping results of the perovskite films prepared by PbI_2 + FAI, δ-$FAPbI_3$ and α-$FAPbI_3$ SCs (film size: 30 cm × 30 cm, measurement region: 40 μm × 40 μm, scale bars: 10 μm). (c) Illustration of the $FAPbI_3$ perovskite solar module structure. (d) *J*–*V* curves for the 30 cm × 30 cm $FAPbI_3$ perovskite solar modules based on PbI_2 + FAI, δ-$FAPbI_3$ and α-$FAPbI_3$ SCs with an aperture area of 663 cm^2 (inset: photograph of the solar module).

presence of spatial inhomogeneity is observed in large-area films based on PbI_2 + FAI precursors, which can be attributed to the random nature of the precursor colloid (Fig. S22†). The uniformity of the precursor colloid size influences the crystallization rate of films in different regions. Such comparison also indicates that the single crystal-based films possess greater scalability than the PbI_2 + FAI mixture (Fig. S23 and S24†). In addition, α-$FAPbI_3$ SC-based perovskite films exhibit the narrowest distribution of PL mapping intensity, which is attributed to the homogeneous control of the colloidal properties in the precursor. The comparison of the total PL intensity distribution between these perovskite films (Fig. S25†) shows that the chemical homogeneity of precursor colloid is of great significance for the overall unity and photoelectric properties of large-area films.

Owing to the high uniformity of the single-crystal precursor, we fabricated 30 cm × 30 cm sized perovskite modules with an aperture area of 663 cm^2 (structure illustrated in Fig. 5c). Table S4† presents the device parameters of PbI_2 + FAI, δ-$FAPbI_3$ and α-$FAPbI_3$ SC-based submodules under reverse scans. As shown in the *J–V* curves in Fig. 5d, PCEs of 19.7% and 20.7% were achieved using δ-$FAPbI_3$ and α-$FAPbI_3$ SCs, respectively. The submodule efficiency based on α-$FAPbI_3$ SCs has been certified to be 20.4% with a V_{oc} of 57.5 V, I_{sc} of 0.302 A, and FF of 77.8% (Fig. S26 and S27†). Meanwhile, the PCEs of the submodules based on PbI_2 + FAI were only 17.6%. More importantly, the α-$FAPbI_3$ SCs used to fabricate the highest module PCE originated from low-purity and low-cost lead iodide, which greatly reduced the commercial cost of the manufacturing process.

Conclusions

In summary, in this work, we investigated and revealed that the colloid behavior of the perovskite precursor varies with the starting materials and can greatly affect photovoltaic performance. The $FAPbI_3$ single-crystal precursor's behavior could exert good control over the chemical composition and colloidal properties, which is more favorable than the traditional PbI_2 + FAI precursor's behavior in terms of phase purity, crystallization orientation, reduced defect density and large-area uniformity for film deposition. By preparing the perovskite single crystals, low-purity materials can also achieve high-performance perovskite photovoltaics, which exhibit an impressive efficiency of 20.7% even in large-area perovskite submodules with a 663 cm^2 aperture area. These findings provide a fundamental understanding of the single-crystal precursor engineering of not only $FAPbI_3$ perovskite but also other solution-based soft-lattice materials in various optoelectronic applications. More importantly, understanding such solution chemistry is beneficial for the scaling-up fabrication of perovskite solar cells, especially for low-cost flow-line production.

Data availability

The data supporting this article have been included as part of the ESI.†

Author contributions

Yugang Liang: data curation, formal analysis, investigation, methodology, writing the original draft, review and editing. Yingping Fan: data curation, formal analysis, investigation. Zhixiao Qin: data curation, investigation. Lei Lu: data curation, validation. Haifei Wang: investigation. Meng Ren: review and editing. Fang Liu: formal analysis. Yanfeng Miao: investigation, review. Yuetian Chen: funding acquisition, methodology, writing and editing. Yixin Zhao: conceptualization, funding acquisition, methodology, supervision, review and editing.

Conflicts of interest

There are no conflicts to declare.

Acknowledgements

This work is supported by the National Natural Science Foundation of China (NSFC, Grant Numbers 22220102002, 22025505, 22209111, 22479098) and the Natural Science Foundation of Shanghai (Grant Number 23ZR1428000). The authors gratefully thank Shanghai Synchrotron Radiation Facility of CAS for the assistance with GIWAXS analysis, and the Instrumental Analysis Centers in Shanghai Jiao Tong University and School of Environmental Science and Engineering for assistance with characterization.

Notes and references

1 J. Burschka, N. Pellet, S.-J. Moon, R. Humphry-Baker, P. Gao, M. K. Nazeeruddin and M. Grätzel, *Nature*, 2013, **499**, 316–319.
2 M. A. Green, A. Ho-Baillie and H. J. Snaith, *Nat. Photonics*, 2014, **8**, 506–514.
3 N. J. Jeon, J. H. Noh, Y. C. Kim, W. S. Yang, S. Ryu and S. I. Seok, *Nat. Mater.*, 2014, **13**, 897–903.
4 Z. Xiao, C. Bi, Y. Shao, Q. Dong, Q. Wang, Y. Yuan, C. Wang, Y. Gao and J. Huang, *Energy Environ. Sci.*, 2014, **7**, 2619–2623.
5 A. Kojima, K. Teshima, Y. Shirai and T. Miyasaka, *J. Am. Chem. Soc.*, 2009, **131**, 6050–6051.
6 J. Park, J. Kim, H.-S. Yun, M. J. Paik, E. Noh, H. J. Mun, M. G. Kim, T. J. Shin and S. I. Seok, *Nature*, 2023, **616**, 724–730.
7 National Renewable Energy Laboratory (NREL), Photovoltaic Research, *Best Research-Cell Efficiency Chart*, 2024, **https://www.nrel.gov/pv/cell-efficiency.html**, accessed 11 October, 2024.
8 H. Chen, C. Liu, J. Xu, A. Maxwell, W. Zhou, Y. Yang, Q. Zhou, A. S. R. Bati, H. Wan, Z. Wang, L. Zeng, J. Wang, P. Serles, Y. Liu, S. Teale, Y. Liu, M. I. Saidaminov, M. Li, N. Rolston, S. Hoogland, T. Filleter, M. G. Kanatzidis, B. Chen, Z. Ning and E. H. Sargent, *Science*, 2024, **384**, 189–193.
9 S. Liu, J. Li, W. Xiao, R. Chen, Z. Sun, Y. Zhang, X. Lei, S. Hu, M. Kober-Czerny, J. Wang, F. Ren, Q. Zhou, H. Raza, Y. Gao, Y. Ji, S. Li, H. Li, L. Qiu, W. Huang, Y. Zhao, B. Xu, Z. Liu,

H. J. Snaith, N.-G. Park and W. Chen, *Nature*, 2024, **632**, 536–542.
10 G. E. Eperon, S. D. Stranks, C. Menelaou, M. B. Johnston, L. M. Herz and H. J. Snaith, *Energy Environ. Sci.*, 2014, **7**, 982–988.
11 H. Lu, Y. Liu, P. Ahlawat, A. Mishra, W. R. Tress, F. T. Eickemeyer, Y. Yang, F. Fu, Z. Wang, C. E. Avalos, B. I. Carlsen, A. Agarwalla, X. Zhang, X. Li, Y. Zhan, S. M. Zakeeruddin, L. Emsley, U. Rothlisberger, L. Zheng, A. Hagfeldt and M. Grätzel, *Science*, 2020, **370**, eabb8985.
12 L. Chao, T. Niu, W. Gao, C. Ran, L. Song, Y. Chen and W. Huang, *Adv. Mater.*, 2021, **33**, 2005410.
13 M. Jung, S.-G. Ji, G. Kim and S. I. Seok, *Chem. Soc. Rev.*, 2019, **48**, 2011–2038.
14 T. D. Siegler, A. Dawson, P. Lobaccaro, D. Ung, M. E. Beck, G. Nilsen and L. L. Tinker, *ACS Energy Lett.*, 2022, **7**, 1728–1734.
15 J. Xu, A. Maxwell, M. Wei, Z. Wang, B. Chen, T. Zhu and E. H. Sargent, *ACS Energy Lett.*, 2021, **6**, 4220–4227.
16 J. Chang, H. Zhu, B. Li, F. H. Isikgor, Y. Hao, Q. Xu and J. Ouyang, *J. Mater. Chem. A*, 2016, **4**, 887–893.
17 J. Yao, L. Yang, F. Cai, Y. Yan, R. S. Gurney, D. Liu and T. Wang, *Sustainable Energy Fuels*, 2018, **2**, 436–443.
18 P. Fassl, V. Lami, A. Bausch, Z. Wang, M. T. Klug, H. J. Snaith and Y. Vaynzof, *Energy Environ. Sci.*, 2018, **11**, 3380–3391.
19 B.-w. Park, N. Kedem, M. Kulbak, D. Y. Lee, W. S. Yang, N. J. Jeon, J. Seo, G. Kim, K. J. Kim, T. J. Shin, G. Hodes, D. Cahen and S. I. Seok, *Nat. Commun.*, 2018, **9**, 3301.
20 Y. Rong, Y. Hu, A. Mei, H. Tan, M. I. Saidaminov, S. I. Seok, M. D. McGehee, E. H. Sargent and H. Han, *Science*, 2018, **361**, eaat8235.
21 J. W. Yoo, E. Noh, J. Jang, K. S. Lee, J. Byeon, M. Choi, J. Im and S. I. Seok, *Joule*, 2023, **7**, 797–809.
22 X. Liu, J. Zhang, H. Wang, Y. Miao, T. Guo, L. K. Ono, S. Yuan, Y. Wang, P. Ji, H. Chen, C. Zhang, T. Li, C. Ding, S. Mariotti, X. Huo, I.-N. Rabehi, H. Wang, Y. Zhao and Y. Qi, *Joule*, 2024, **8**, 2851–2862.
23 T. Bu, J. Li, H. Li, C. Tian, J. Su, G. Tong, L. K. Ono, C. Wang, Z. Lin, N. Chai, X.-L. Zhang, J. Chang, J. Lu, J. Zhong, W. Huang, Y. Qi, Y.-B. Cheng and F. Huang, *Science*, 2021, **372**, 1327–1332.
24 T. Bu, L. K. Ono, J. Li, J. Su, G. Tong, W. Zhang, Y. Liu, J. Zhang, J. Chang, S. Kazaoui, F. Huang, Y.-B. Cheng and Y. Qi, *Nat. Energy*, 2022, **7**, 528–536.
25 Y. Miao, M. Ren, Y. Chen, H. Wang, H. Chen, X. Liu, T. Wang and Y. Zhao, *Nat Sustainability*, 2023, **6**, 1465–1473.
26 G. Zhang, B. Ding, Y. Ding, Y. Liu, C. Yu, L. Zeng, Y. Wang, X. Zhang, M. Liu, Q. Tian, B. Fan, Q. Liu, G. Yang, M. K. Nazeeruddin and B. Chen, *Sci. Adv.*, 2024, **10**, eadl6398.
27 D.-N. Jeong, D.-K. Lee, S. Seo, S. Y. Lim, Y. Zhang, H. Shin, H. Cheong and N.-G. Park, *ACS Energy Lett.*, 2019, **4**, 1189–1195.
28 W. Feng, J. Tao, G. Liu, G. Yang, J.-X. Zhong, Y. Fang, L. Gong, S. Yang and W.-Q. Wu, *Angew. Chem., Int. Ed.*, 2023, **62**, e202300265.
29 K. Wang, C. Wu, Y. Hou, D. Yang, T. Ye, J. Yoon, M. Sanghadasa and S. Priya, *Energy Environ. Sci.*, 2020, **13**, 3412–3422.
30 J. Jeong, M. Kim, J. Seo, H. Lu, P. Ahlawat, A. Mishra, Y. Yang, M. A. Hope, F. T. Eickemeyer, M. Kim, Y. J. Yoon, I. W. Choi, B. P. Darwich, S. J. Choi, Y. Jo, J. H. Lee, B. Walker, S. M. Zakeeruddin, L. Emsley, U. Rothlisberger, A. Hagfeldt, D. S. Kim, M. Grätzel and J. Y. Kim, *Nature*, 2021, **592**, 381–385.
31 M. Kim, I.-w. Choi, S. J. Choi, J. W. Song, S.-I. Mo, J.-H. An, Y. Jo, S. Ahn, S. K. Ahn, G.-H. Kim and D. S. Kim, *Joule*, 2021, **5**, 659–672.
32 L. He, H. Gu, X. Liu, P. Li, Y. Dang, C. Liang, L. K. Ono, Y. Qi and X. Tao, *Matter*, 2020, **2**, 167–180.
33 Y. Qin, H. Zhong, J. J. Intemann, S. Leng, M. Cui, C. Qin, M. Xiong, F. Liu, A. K. Y. Jen and K. Yao, *ACS Energy Lett.*, 2020, **10**, 1904050.
34 S. Sidhik, W. Li, M. H. K. Samani, H. Zhang, Y. Wang, J. Hoffman, A. K. Fehr, M. S. Wong, C. Katan, J. Even, A. B. Marciel, M. G. Kanatzidis, J.-C. Blancon and A. D. Mohite, *Adv. Mater.*, 2021, **33**, 2007176.
35 E. H. Jung, N. J. Jeon, E. Y. Park, C. S. Moon, T. J. Shin, T.-Y. Yang, J. H. Noh and J. Seo, *Nature*, 2019, **567**, 511–515.
36 G. Kim, H. Min, S. Lee Kyoung, Y. Lee Do, M. Yoon So and I. Seok Sang, *Science*, 2020, **370**, 108–112.
37 X. Zheng, Y. Hou, C. Bao, J. Yin, F. Yuan, Z. Huang, K. Song, J. Liu, J. Troughton, N. Gasparini, C. Zhou, Y. Lin, D.-J. Xue, B. Chen, A. K. Johnston, N. Wei, M. N. Hedhili, M. Wei, A. Y. Alsalloum, P. Maity, B. Turedi, C. Yang, D. Baran, T. D. Anthopoulos, Y. Han, Z.-H. Lu, O. F. Mohammed, F. Gao, E. H. Sargent and O. M. Bakr, *Nat. Energy*, 2020, **5**, 131–140.
38 Y. Zhang, S. Seo, S. Y. Lim, Y. Kim, S.-G. Kim, D.-K. Lee, S.-H. Lee, H. Shin, H. Cheong and N.-G. Park, *ACS Energy Lett.*, 2020, **5**, 360–366.
39 G. Tong, D.-Y. Son, L. K. Ono, H.-B. Kang, S. He, L. Qiu, H. Zhang, Y. Liu, J. Hieulle and Y. Qi, *Nano Energy*, 2021, **87**, 106152.
40 T. Zhang, M. Yang, E. E. Benson, Z. Li, J. van de Lagemaat, J. M. Luther, Y. Yan, K. Zhu and Y. Zhao, *Chem. Commun.*, 2015, **51**, 7820–7823.
41 M. I. Saidaminov, A. L. Abdelhady, B. Murali, E. Alarousu, V. M. Burlakov, W. Peng, I. Dursun, L. Wang, Y. He, G. Maculan, A. Goriely, T. Wu, O. F. Mohammed and O. M. Bakr, *Nat. Commun.*, 2015, **6**, 7586.
42 P. Zhu, D. Wang, Y. Zhang, Z. Liang, J. Li, J. Zeng, J. Zhang, Y. Xu, S. Wu, Z. Liu, X. Zhou, B. Hu, F. He, L. Zhang, X. Pan, X. Wang, N.-G. Park and B. Xu, *Science*, 2024, **383**, 524–531.
43 Q. Gao, J. Qi, K. Chen, M. Xia, Y. Hu, A. Mei and H. Han, *Adv. Mater.*, 2022, **34**, 2200720.
44 H. Li, N. Shen, S. Chen, F. Guo and B. Xu, *Adv. Funct. Mater.*, 2023, **33**, 2214339.
45 J. T.-W. Wang, Z. Wang, S. Pathak, W. Zhang, D. W. deQuilettes, F. Wisnivesky-Rocca-Rivarola, J. Huang, P. K. Nayak, J. B. Patel, H. A. Mohd Yusof, Y. Vaynzof, R. Zhu, I. Ramirez, J. Zhang, C. Ducati, C. Grovenor,

M. B. Johnston, D. S. Ginger, R. J. Nicholas and H. J. Snaith, *Energy Environ. Sci.*, 2016, **9**, 2892–2901.
46 J.-W. Lee, S. Tan, T.-H. Han, R. Wang, L. Zhang, C. Park, M. Yoon, C. Choi, M. Xu, M. E. Liao, S.-J. Lee, S. Nuryyeva, C. Zhu, K. Huynh, M. S. Goorsky, Y. Huang, X. Pan and Y. Yang, *Nat. Commun.*, 2020, **11**, 5514.
47 K. Yan, M. Long, T. Zhang, Z. Wei, H. Chen, S. Yang and J. Xu, *J. Am. Chem. Soc.*, 2015, **137**, 4460–4468.
48 R. J. Stewart, C. Grieco, A. V. Larsen, G. S. Doucette and J. B. Asbury, *J. Phys. Chem. C*, 2016, **120**, 12392–12402.
49 K. G. Stamplecoskie, J. S. Manser and P. V. Kamat, *Energy Environ. Sci.*, 2015, **8**, 208–215.
50 A. Sharenko, C. Mackeen, L. Jewell, F. Bridges and M. F. Toney, *Chem. Mater.*, 2017, **29**, 1315–1320.
51 Y. Deng, C. H. Van Brackle, X. Dai, J. Zhao, B. Chen and J. Huang, *Sci. Adv.*, 2019, **5**, eaax7537.
52 J. Kim, B.-w. Park, J. Baek, J. S. Yun, H.-W. Kwon, J. Seidel, H. Min, S. Coelho, S. Lim, S. Huang, K. Gaus, M. A. Green, T. J. Shin, A. W. Y. Ho-baillie, M. G. Kim and S. I. Seok, *J. Am. Chem. Soc.*, 2020, **142**, 6251–6260.
53 L. Chao, Y. Xia, B. Li, G. Xing, Y. Chen and W. Huang, *Chem*, 2019, **5**, 995–1006.
54 H. Min, S.-G. Ji and S. I. Seok, *Joule*, 2022, **6**, 2175–2185.
55 F.-C. Chen, J.-L. Wu, C.-L. Lee, Y. Hong, C.-H. Kuo and M. H. Huang, *Appl. Phys. Lett.*, 2009, **95**, 013305.
56 Y. Wang, M. Feng, H. Chen, M. Ren, H. Wang, Y. Miao, Y. Chen and Y. Zhao, *Adv. Mater.*, 2024, **36**, 2305849.